

Experimental investigations and large-eddy simulation of low-swirl combustion in a lean premixed multi-nozzle combustor

W. J. Liu · B. Ge · Y. S. Tian · Y. W. Yuan · S. S. Zang · S. L. Weng

Received: 1 October 2014 / Revised: 23 December 2014 / Accepted: 23 December 2014 / Published online: 1 February 2015
© Springer-Verlag Berlin Heidelberg 2015

Abstract This paper presents laser diagnostic experiments and large-eddy simulations (LES) of low-swirl lean premixed methane/air flames in a multi-nozzle combustor including five nozzles with the same structure. OH planar laser-induced fluorescence is used to observe flame shapes and identify main reaction zones. NO_x and CO emissions are also recorded during the experiment. The flows and flames are studied at different equivalence ratios ranging from 0.5 to 0.8, while the bulk inlet velocity is fixed at 6.2 m/s. Results show that the neighboring swirling flows interact with each other, generating a highly turbulent interacting zone where intensive reactions take place. The flame is stabilized above the nozzle rim, and its liftoff height decreases with increasing equivalence ratio. The center flow is confined and distorted by the neighboring flows, resulting in instabilities of the center flame. Mean OH radical images reveal that the center nozzle flame is extinguished when equivalence ratio is equals to 0.5, which is successfully predicted by LES. In addition, NO_x emissions show log-linear dependency on the adiabatic flame temperature, while the CO emissions remain lower than 10 ppm. NO_x emissions for multi-nozzle flame are less sensitive to the flame temperature than that for single nozzle. These results demonstrate that the low-swirl multi-nozzle concept is a promising solution to achieve stable combustion with ultra-low emissions in gas turbines.

1 Introduction

Dry low NO_x (DLN) combustion is widely employed due to the more and more stringent emission demands. Among all of the DLN combustion methods, a new combustion technology called low-swirl combustion (LSC) is a promising way to achieve those emission demands. LSC is an aerodynamic flame stabilization method originally developed at the Lawrence Berkeley National Laboratory. The swirl number for LSC is commonly between 0.4 and 0.55 (Chan et al. 1992; Cheng 1995; Cheng et al. 2001). It is a simple, robust, and readily adaptable technology for gas turbine combustors to meet strict emissions targets without significantly altering their system configurations, efficiencies, and turndown (Cheng 2006). Johnson et al. (2005) reported that the flowfields of the LSC are devoid of a large dominant recirculation zone. The flow diverges at the nozzle exit, forming a low velocity zone, which favors flame stabilization. The flame sits at the position where turbulent flame speed equals to local velocity (Day et al. 2012). This is fundamentally different than the strong and large recirculation regions that dominate flowfields of the traditional high-swirl combustion (HSC). Its NO_x emissions are about 60 % lower than the HSC, while its CO emissions are comparable. Nogenmyr et al. (2009) numerically and experimentally revealed several intrinsic features of the single low-swirl flame at a low Reynolds number, such as the W-shape at the leading front, the highly wrinkled fronts in the shear layers, and the existence of extinction holes in the trailing edge of the flame.

However, in real heavy duty gas turbine combustors, multi-nozzle combustion technology is widely used. Multi-nozzle combustion has the advantage of combustion noise inhibition and suppression of thermoacoustic oscillation. Boehm et al. (2007) performed experimental investigations

W. J. Liu · B. Ge · Y. S. Tian · Y. W. Yuan · S. S. Zang (✉) · S. L. Weng
School of Mechanical Engineering, Shanghai Jiao Tong University, Dongchuan Road 800, Shanghai 200240, China
e-mail: sszang@sjtu.edu.cn

W. J. Liu
e-mail: zhanshen@sjtu.edu.cn

of turbulence structure in a three-nozzle combustor. Results showed that the size and shape of the internal recirculation zones were significantly influenced by operation of adjacent nozzles. Szedlmayer et al. (2011) conducted experiments on forced flame response in a five-nozzle lean premixed gas turbine can combustor. Kim et al. (2010) reported periodical pressure distribution in an annular combustor with multiple swirl injectors by large-eddy simulations (LES) and proper orthogonal decomposition method. Cai et al. (2001, 2002) and Lannetti et al. (2001) studied the characteristics of a rotating flow generated by two different swirler configurations with multiswirlers arrays. Worth and Dawson (2012) conducted an experimental investigation into the interactions that occur between two lean premixed flames under unforced and acoustic forced circumstances. Results showed that the occurrence of jet/flame merging has effect on the local flame interactions in the unforced flames and the vortex–flame interactions of the forced flames. Table 1 summarizes the differences between present work and previous multi-nozzle combustion studies. It shows that the multi-nozzle combustors are generally can or annular type with nozzle distance ranging from 1.1 to $4.3D$, where D is the nozzle diameter. The configurations of multi-nozzle combustors in terms of the number of nozzles and nozzles arrangement are different from each other due to the different type of combustors been studied. The main difference between current study and the previous works is that the multi-nozzle combustion is stabilized with low-swirl flow motion, which is rarely reported.

Smith et al. (2010) performed a fuel flexible combustor conceptual design using low-swirl multi-nozzle combustion technology and discussed the requirements for the fuel handling and delivery circuit. Nazeer et al. (2006) conducted combustion experiment in production annular gas turbine combustor using a set of injectors. Rig testing also demonstrated the ultra-low NO_x capability of the injectors on natural gas. Those two studies have already demonstrated that it is possible to adopt low-swirl combustion technology in multi-nozzle gas turbine combustor, however, lacking the analysis of interacting mechanism between neighboring flames.

Since the interaction between neighboring flows and flames would dramatically change the flowfield and combustion process, it is necessary to gain a fundamental knowledge of low-swirl multi-nozzle combustion. In this paper, we construct a multi-nozzle model combustor including five low-swirl nozzles of the same configuration. Laser diagnostic experiments and large-eddy simulations are performed on the combustor. The objective of this study was to provide a preliminary understanding of the physical and flame processes in the low-swirl multi-nozzle combustor. Particular emphasis is placed on their mutual interactions between neighboring nozzles. The effect of equivalence ratio on neighboring flame interaction is also discussed.

2 Experimental details

2.1 Nozzle structure and arrangement

The structure of a single element low-swirl nozzle used in this investigation is shown in Fig. 1. The low-swirl nozzle comprises of a nozzle pipe with an inner diameter of 34 mm and a swirler placed 36 mm upstream of the exit plane. The annular section of the swirler is fitted with eight constant thickness curved vanes, each having a discharge angle of 37° . The central channel is 24 mm in diameter and is fitted with a perforated plate that has 30 holes of 2 mm in diameter. This swirler configuration proposed by Petersson et al. (2011) allows a portion of the premixed gas passing through the annular section keeping swirling while the rest gas flows through the open center channel remaining un-swirled.

From Cheng et al. (2009), the definition of geometric swirler number, S , is

$$S = \frac{2}{3} \tan \alpha \frac{1 - R^3}{1 - R^2 + \left[m^2 (1/R^2 - 1)^2 \right] R^2} \quad (1)$$

where α is the vane angle and $R = R_c/R_b$. m is the ratio of mass flux through center channel to swirl annulus. Non-reacting flow simulation for single nozzle was performed previously. It showed that about 30 % flow by mass passed

Table 1 Differences between present work and related multi-nozzle combustion studies

Author	Swirl number	Number of nozzles	Nozzles arrangement	Combustor type	Distance between nozzles (D)	Reacting or NOT	Exp. or comp.
Cai	–	9	Three by three	Square	1.4	NOT	E (LDV)
Boehm	1	3	Linear	Annular (segment)	4.3	NOT	E (LDV)
Worth	0.87	2	Side by side	Rectangle	1.14–2.0	Reacting	E (PLIF)
Szedlmayer	0.78	5	Four around one	Can	1.2	Reacting	E (3D imaging)
Kim	0.56	3	Side by side	Annular (segment)	2.1	Reacting	C (LES)
Present work	0.55	5	Four around one	Can	2.0	Reacting	E&C (PLIF&LES)

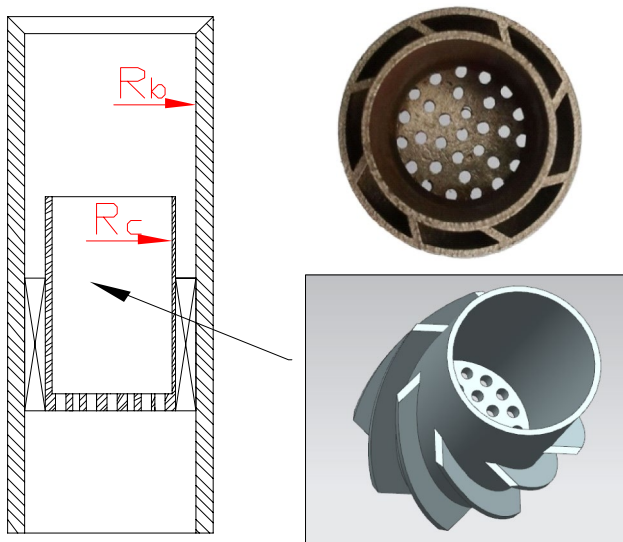


Fig. 1 Schematic of the structure of a single element low-swirl nozzle

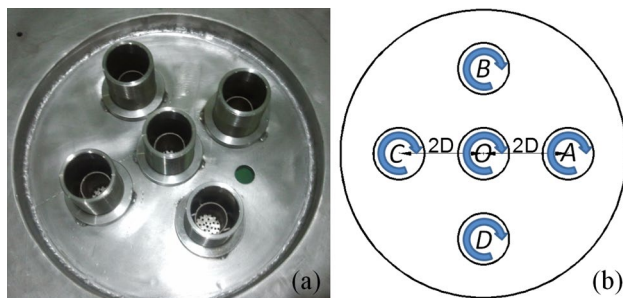


Fig. 2 Multi-nozzle arrangement

through the perforated plate. Thus, according to the definition of S , we can determine that the swirl number of this swirler is 0.55.

The port configuration of multi-nozzle combustor shown in Fig. 2a consists of five low-swirl nozzles with the same structure mentioned above. The five nozzles are arrayed in a right angle cross-configuration with Nozzle O , in the center surrounded by the other four nozzles, Nozzle A to D , as shown in Fig. 2b. All five swirlers have the same swirling direction. The distance between the central nozzle and the outer ones is $2D$, where D is the nozzle diameter of 41 mm. In order to eliminate the effect of vortices at the bottom of the nozzles on the combustion performance, the five nozzles extend into the combustor for 45.5 mm.

2.2 The test rig

The experiments are carried out on an atmospheric pressure combustion performance test rig at Shanghai Jiao

Tong University shown schematically in Fig. 3. The system includes a combustion subsystem, a gas fuel (CH_4) supply subsystem, an air supply subsystem, and a gas analysis subsystem.

The combustion subsystem is mainly comprised of a premixer, a premixed gas chamber, five arrayed nozzles, cylindrical model combustor, and exhaust section. The methane and air are well mixed in the premixer before delivering to the large gas chamber, which is used to keep the nozzle inlet pressure stable. The optically accessible combustor is made of quartz with a diameter of 290 mm and a length of 200 mm. After burning in the combustor, the burned gas is exhausted into the water-cooled exhaust section (not shown in Fig. 3).

We use a gas mass flow controller (MFC) to measure and control methane mass flow. The air flow rate is controlled by a flowmeter and transducer. In addition, the emissions at the exhaust section are measured by Siemens gas analyzer (ULTRAMAT 23). The NO_x and CO emissions are converted to the concentrations at 15 % O_2 condition with the O_2 concentration recorded simultaneously.

Planar laser-induced fluorescence (PLIF) of OH radical is employed to detect reaction zone dimension and flame front position. The excitation laser derives from a pulsed Nd: YAG laser pumping a tunable dye laser with Rhodamine 6G as dye solution before going through a frequency double crystal. The output ultraviolet laser beam has the wavelength of 281.46 nm with pulse duration of 20 ns at the power of 70 mW and is used to excite OH radicals on the $R1(9)$ line of the $A^2\Sigma^+ \leftarrow X^2\Pi(v' = 1, v'' = 0)$ transition 16. The ultraviolet laser beam is expanded by a set of spherical and cylindrical lenses, forming a laser sheet with the thickness $<500 \mu\text{m}$. The laser sheet is guided vertically through the center of the test section in the combustion chamber. The fluorescence is then collected around wavelength of 310 nm by an ICCD camera placed perpendicular to the laser sheet plane with Nikon UV lens, in front of which a combined UG11 and WG305 interference filter set is installed to suppress scattered laser light and background flame radiation. Timing delay of PLIF system is controlled by a pulse delay generator DG535. The gate width or exposure time of ICCD camera is set to 50 ns to include a complete OH fluorescence for each instantaneous laser shot. Five hundred single-shot OH-PLIF raw images are recorded for post-processing for each flame. PLIF measurement field, $100 \times 100 \text{ mm}^2$ rectangular test section, is fixed to the exit of the swirler. The resolution of each image is higher than 0.1 mm per pixel.

During the experiments, keeping the bulk inlet velocity for each nozzle constant, 6.2 m/s, the flow rate of the methane and air was modified simultaneously to change equivalence ratio, ϕ , from 0.5 to 0.8. The operation conditions are listed in Table 2. The temperature of air/fuel mixture is

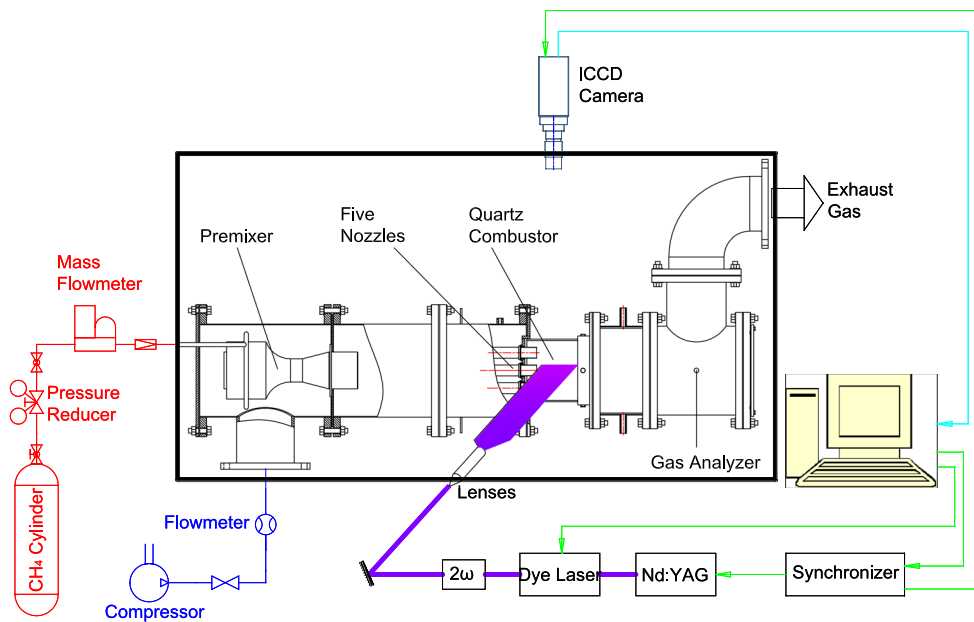


Fig. 3 Schematic of the test rig system

Table 2 Operation conditions and mixture properties

ϕ	CH ₄ (L/min)	Air (m ³ /h)	T_{ad} (K)	S_L (cm/s)	Heat load (kW)
0.5	84.3	96.3	1,480	–	45.82
0.6	100.1	95.3	1,666	10.75	54.44
0.7	115.7	94.4	1,838	19.05	62.89
0.8	130.9	93.5	1,996	27.00	71.18

294.6 K, and the inlet Reynolds number is about 13,300 for each condition. The mixture properties, such as the adiabatic flame temperature, T_{ad} , and laminar flame speeds, S_L , are determined from the “premix” module of CHEMKIN using GRI 3.0 mechanism.

3 Numerical method

3.1 Governing equations

The governing equations for LES are obtained by filtering the time-dependent Navier–Stokes equations. With the filter function, $G(x, x')$,

$$G(x, x') = \begin{cases} 1/V, & x \in v \\ 0, & x' \text{ otherwise} \end{cases} \quad (2)$$

where V is the volume of a computational cell, the governing equations of mass, momentum, and energy can be written as (Kim et al. 2010):

$$\frac{\partial \bar{\rho}}{\partial t} + \frac{\partial}{\partial x_i} (\bar{\rho} \tilde{u}_i) = 0 \quad (3)$$

$$\frac{\partial (\bar{\rho} \tilde{u}_i)}{\partial t} + \frac{\partial}{\partial x_i} (\bar{\rho} \tilde{u}_i \tilde{u}_j + \bar{P} \delta_{ij} - \bar{\tau}_{ij} + \tau_{ij}^{sgs}) = 0 \quad (4)$$

$$\frac{\partial (\bar{\rho} \tilde{E})}{\partial t} + \frac{\partial}{\partial x_i} [(\bar{\rho} \tilde{E} + \bar{P}) \tilde{u}_i + \bar{q}_i - \tilde{u}_j \bar{\tau}_{ij} + H_i^{sgs} + \sigma_{ij}^{sgs}] = 0 \quad (5)$$

where the subscripts i, j are the spatial coordinate index. τ_{ij} and q_i are the viscous stress tensor and heat flux, respectively. The unresolved subgrid scale (sgs) closure terms are given by:

$$\tau_{ij}^{sgs} = (\overline{\rho u_i u_j} - \bar{\rho} \tilde{u}_i \tilde{u}_j) \quad (6)$$

$$H_i^{sgs} = (\overline{\rho E u_i} - \bar{\rho} \tilde{E} \tilde{u}_i) + (\overline{P u_i} - \bar{P} \tilde{u}_i) \quad (7)$$

$$\sigma_{ij}^{sgs} = (\overline{u_j \tau_{ij}} - \tilde{u}_j \bar{\tau}_{ij}) \quad (8)$$

The sgs turbulent stress is modeled using the compressible version of the Smagorinsky model (Erlebacher et al. 1992), given as:

$$\tau_{ij}^{sgs} = -2\nu_t \bar{\rho} \left(\tilde{S}_{ij} - \frac{\tilde{S}_{kk} \delta_{ij}}{3} \right) + \frac{2}{3} \bar{\rho} k^{sgs} \delta_{ij} \quad (9)$$

where \tilde{S}_{ij} is the rate of strain tensor,

$$\tilde{S}_{ij} = \frac{1}{2} \left(\frac{\partial \tilde{u}_i}{\partial x_j} + \frac{\partial \tilde{u}_j}{\partial x_i} \right) \quad (10)$$

$$\nu_t = D_R \Delta^2 \left(2\tilde{S}_{ij}\tilde{S}_{ij} \right)^{0.5} \tag{11}$$

$$k^{sgs} = C_I \Delta^2 \left(2\tilde{S}_{ij}\tilde{S}_{ij} \right) \tag{12}$$

where the dimensionless constants, C_R and C_I , determined empirically, represent the compressible Smagorinsky constants.

The sgs energy flux, H_i^{sgs} , is modeled as

$$H_i^{sgs} = -\bar{\rho} \frac{\nu_t}{Pr_t} \frac{\partial \tilde{h}}{\partial x_i} \tag{13}$$

where \tilde{h} is the resolved sgs total enthalpy, given by:

$$\tilde{h} = \tilde{E} + \frac{\tilde{P}}{\bar{\rho}} \tag{14}$$

3.2 Partially premixed combustion model

The partially premixed model (Biagioli et al. 2008) solves a transport equation for the mean reaction progress variable, \bar{c} and the mean mixture fraction, \bar{f} , as well as the mixture fraction variance, $\overline{f'^2}$. Ahead of the flame ($c = 0$), the fuel and oxidizer are mixed but unburnt, and behind the flame ($c = 1$), the mixture is burnt.

Density weighted mean scalars, $\bar{\gamma}$, such as species fractions and temperature, are calculated from the probability density function (PDF) of f and c as:

$$\bar{\gamma} = \int_0^1 \int_0^1 \gamma(f, c) p(f, c) df dc \tag{15}$$

Under the assumption of thin flames, so that only unburnt reactants and burnt products exist, the mean scalars are determined from

$$\bar{\gamma} = \bar{c} \int_0^1 \gamma_b(f) p(f) df + (1 - \bar{c}) \int_0^1 \gamma_u(f) p(f) df \tag{16}$$

where the subscripts b and u denote burnt and unburnt, respectively.

The burnt scalars, γ_b , are functions of the mixture fraction and are calculated by mixing a mass f of fuel with a mass $(1 - f)$ of oxidizer and allowing the mixture to equilibrate. The unburnt scalars, γ_u , are calculated similarly, but the mixture is not reacted.

3.3 Numerical procedure

Figure 4 shows a schematic of the computational domain including five low-swirl nozzles, 34 mm diameter for each nozzle, and the length of the combustor is 400 mm. In order to simplify the mesh construction, flows through the swirlers are not simulated. Instead, the swirler inlets are

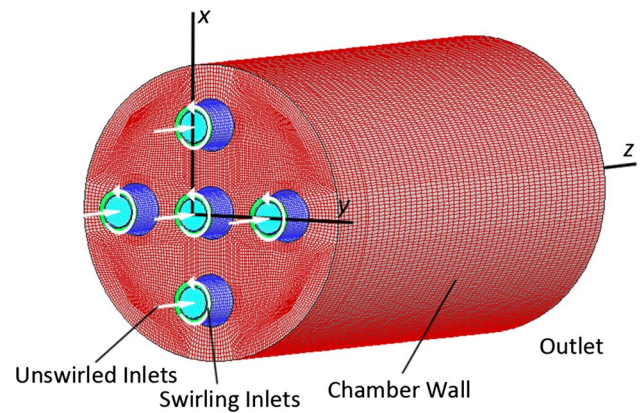


Fig. 4 Schematic of computational mesh and boundary conditions

simplified as an inner part without swirl and an outer with swirl.

The operation conditions are pressure 1 atm, inlet temperature 295 K, and the inlets of the center and annular part of the swirlers are specified with fixed mass flows based on experimental data. Each nozzle has the same swirling direction in accordance with experimental configuration.

LES is performed for operation conditions listed in Table 2. The governing equations are solved numerically by means of a finite-volume approach, which allows for the treatment of arbitrary geometry. A second-order central-differencing scheme is employed for spatial discretization. Temporal discretization is obtained using a second-order implicit scheme. Each snapshot was saved in every 50 μ s.

During the numerical calculation, once the combustion model, sgs model and discretization scheme are determined, the accuracy of numerical results mainly relies on the grid resolution. Coarse grids reduce the accuracy of the results, while over-fine grids make the LES approach close to DNS, however, increasing the computational cost. It is necessary to find a reasonable grid resolution that both meet the accuracy criteria and the low computational cost demand. So, grid dependence validation is performed to ensure that the results are not substantially affected by the grid size. Three different meshes with 6, 7.1 and 8.2 million cells were tested. Figure 5 shows the iso-vorticity of 2,400 s^{-1} distribution with different grid resolutions. It can be found that the medium and dense grids can well reproduce the major vorticities in the multi-swirling flowfield, while the coarse grid fails to predict enough vorticities compared to the other two cases.

Apart from the similar vorticity distribution predicted by the two largest meshes in Fig. 5, the time-averaged axial velocity shown in Fig. 6 also suggests that the coarse mesh has a large disagreement. Taking the computational cost into account, the 6 million cell mesh with a grid size of 2 mm was chosen in this work.

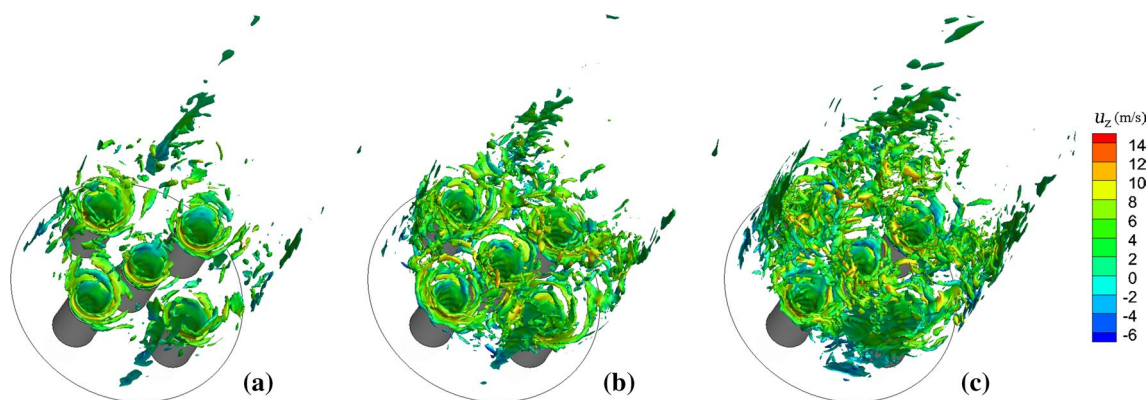


Fig. 5 Iso-vorticity magnitude distribution with different grid resolutions. **a** 6 M; **b** 7.1 M; **c** 8.2 M

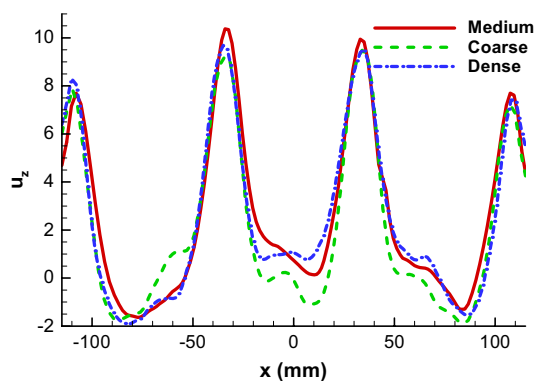


Fig. 6 Mean axial velocity profiles at $z = 134$ mm with different grid resolutions

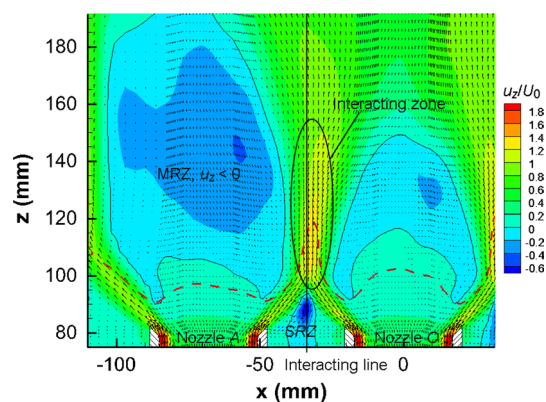


Fig. 7 Mean flowfield for CH_4 multi-nozzle flames at $U_0 = 6.2$ m/s and $\phi = 0.6$ from LES (red dash line marks the flame front)

4 Results and discussion

4.1 Mean flow structure analysis

Obviously, the flowfield in a multi-nozzle combustor is more complex than that in a single-nozzle combustion chamber due to the interaction between neighboring nozzles. We begin by examining the characteristic of the low-swirl multi-nozzle flow structure using the LES obtained at a bulk inlet velocity of $U_0 = 6.2$ m/s and CH_4/air at $\phi = 0.6$.

Figure 7 shows the mean flowfield on the $y = 0$ plane. Both the center nozzle, Nozzle O, and the neighboring nozzle, Nozzle A, have the similar flow patterns. For each single nozzle, the center part un-swirling flow is relatively slow, forming a low velocity zone favors flame stabilization, while the outer part flow imparting tangential swirling with high velocity magnitude generates a divergent flow at nozzle exit. The deceleration of velocity at the centerline is outlined by contours of the normalized axial velocity, u_z/U_0 . Central Main Recirculation Zones (MRZ) typical for swirling flows are formed at the downstream of the nozzle

exits. The formation of the weak central recirculation zone is outlined by the $u_z = 0$ contour. It can be seen that the shapes of the MRZ's above center nozzle and outer Nozzle A are quite different. The size of MRZ above Nozzle A is larger than that above center nozzle. This indicates that the center nozzle flow is confined by the neighboring flows from the outer nozzles, altering the size and strength of the recirculation zone as it would be established for a single-nozzle flow. In addition, Secondary Recirculation Zones (SRZ) between the adjacent nozzle lips are formed due to the entrainment of high velocity of the outer part swirling flows. The forming of SRZs would result in high temperature in this region being harmful to the safe operation of the nozzles. This will be discussed in the next section.

At the outlet of each nozzle in the relatively thin zone of high positive axial velocity, two shear layers are produced: an inner one between the MRZ and the nozzle flow, and an outer one between the nozzles flow and the ambient flow.

The swirling flows of center nozzle radial expansion merge at $x \approx \pm 34$ mm with the swirling flows of the outer

nozzles, forming a high velocity interacting zone shown in Fig. 7. Red dash lines mark the flame fronts showing that the individual flame has “W” shape similar to the one reported by Nogenmyr et al. (2009). The MRZs are mainly formed at the downstream of the flame front, which suggests that the weak recirculation zones do not play an important role in flame stabilization.

Normalized velocity distributions at different height above the burner are shown in Fig. 8. In Fig. 8a, we can clearly find the SRZs between neighboring nozzles and outer part high axial velocity flow for each nozzle at the nozzle exit position. As $H = 2D$ shown in Fig. 8b, where H is the axial distance to the burner exit, we can find a elliptic ring-shape high velocity region for each outer nozzle, and a square-shape confined interacting region for center nozzle owing to the merging of the neighboring flows. At further downstream location, the center flow is more distorted. The interesting phenomenon at this axial location is that the mean axial velocity distributions generated by the four outer nozzles are not axially symmetric around its own center. The locations of the maximum axial velocity are biased to the swirling direction. This indicates that the flow above each nozzle is not only from its

own swirler but also has contributions from the neighboring swirlers. When $H = 4D$, the MRZs for all five nozzles are eliminated and the flows become more uniform.

Centerline profiles of mean axial velocity (upper) and scaled turbulent intensity are shown in Fig. 9. As shown in Fig. 9a, the decay of u_z/U_0 for all three nozzles in the near-field (about $H/D < 0.5$) is linear and the slopes of decay, $dU/dx/U_0$, keep the same value. As H increases, the axial velocity becomes negative, which means recirculation zone occurs. From the axial velocity distribution below zero dash line, we can infer that the MRZs for Nozzle A and C are much larger than that for center nozzle. This validates that the center flow is squeezed by the outer nozzle flows, but do not alter the self-similar behavior.

Axial profiles of the scaled turbulent intensity, q'/U_0 , are shown in Fig. 9b. In the nearfield before merging, the turbulent intensity levels within the reactants increase as H increases and the flow fluctuations are similar. In the far-field, the significant increase in q'/U_0 is observed for all nozzles and the fluctuations of center nozzle are smaller than neighboring nozzles. This is resulted from the confinement of the outer flows far downstream.

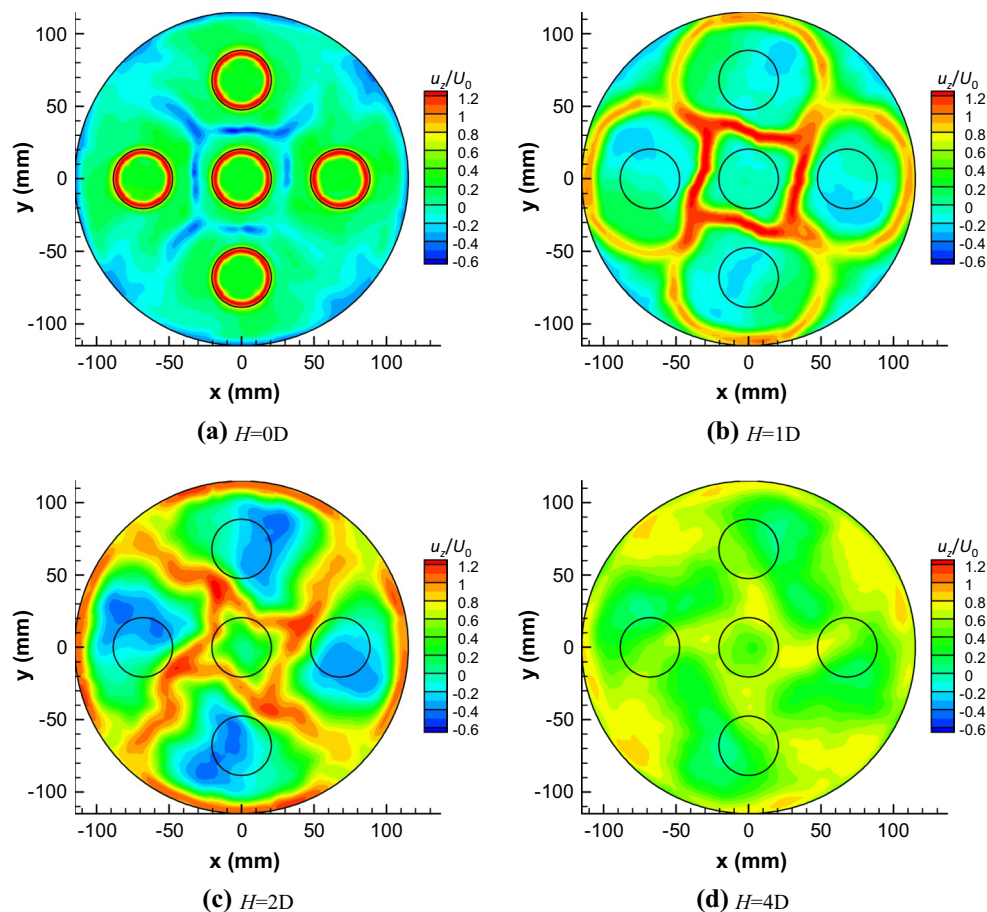


Fig. 8 Normalized velocity distribution for $U_0 = 6.2$ m/s and $\phi = 0.6$ at different height above the burner

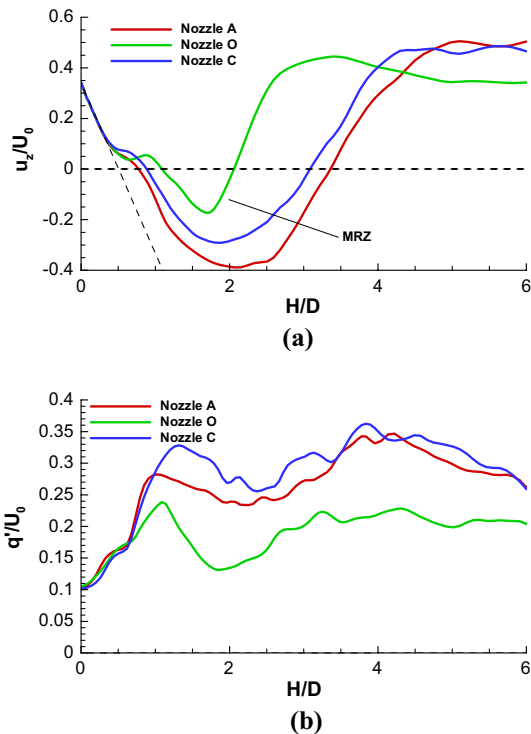


Fig. 9 Centerline profiles of mean axial velocity (*upper*) and fluctuations (*lower*) for CH₄/air flames of $U_0 = 6.2$ m/s and $\phi = 0.6$

In order to facilitate the analysis of the interacting flow between two neighboring nozzles, the interacting line at $x = -34$ mm is defined. Figure 10 shows the profiles of the mean axial velocity and the normalized turbulent intensity along the interacting line.

Note that the flow along the interacting line is quite different from the centerline. The negative velocity means the SRZ. The axial velocity increases significantly to a high value as the flow passes the stagnant point. It means that the interacting of the neighboring flow accelerates the local velocity in the interacting zone.

The flow along interacting line seems to be more turbulent shown in Fig. 10b. The fluctuations along the interacting line have two peaks for all equivalence ratios. The first peak represents the high turbulence in the SRZ, while the second peak value is produced by the interacting of the outer swirling flows from neighboring nozzles.

4.2 Characteristics of multi-nozzle flames

4.2.1 Instantaneous flame structure

Instantaneous distribution of OH concentration and velocity vector obtained from LES, as well as a snap shot of OH-PLIF, are shown in Fig. 11. Since PLIF gives only

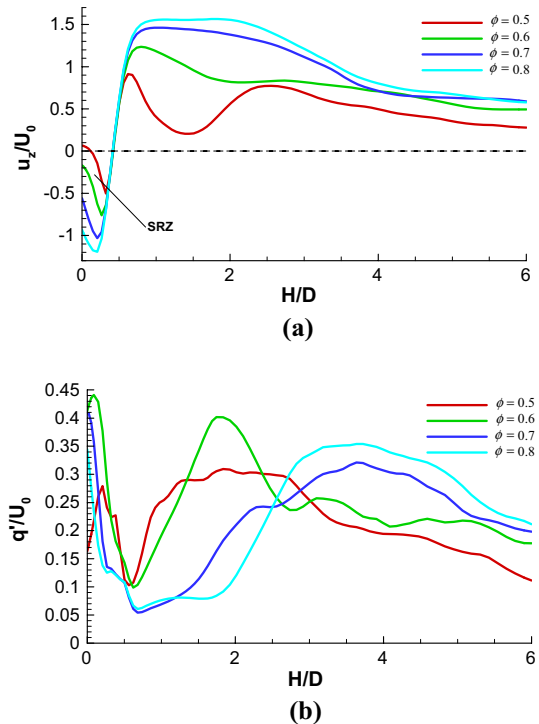


Fig. 10 Profiles of mean axial velocity (*upper*) and fluctuations (*lower*) along interacting line for different equivalence ratios

relative signals, there has been no attempt to evaluate the quantitative scale of the OH field. The left flame is the outer flame settling at a position downstream of Nozzle A, while the right flame is the center flame stabilized above Nozzle O. The neighboring two flames interact with each other, producing different shapes of OH distributions. We can find that the OH distributions of the outer flame are wider than the center flame from both LES and PLIF results.

In the vicinity of nozzle exit, both flowfields exhibit the characteristic features of divergent flows with the flow expanding radially and the axial velocity decreasing with increasing z . To the left of the center nozzle shown in Fig. 11a, two large vortices are seen in the inner shear layers. There are a few regions in the flame front where the OH concentration has a peak (presented in red color).

Figure 11b shows a snap shot of OH-PLIF of two premixed low-swirl flames. The red line is deduced from the maximum gradient of OH signal, which is an approximate representation of the flame front. The flame front is highly wrinkled, and the wrinkle sizes are much smaller than the LES results. There exist lots of flame cusps at the flame front, especially in the interacting zone where OH signal has a higher value. The OH signal of the center flame is lower than that of the outer flame, which is opposite to the numerical prediction.

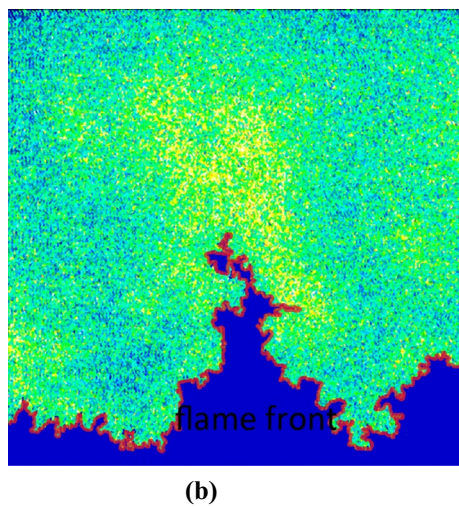
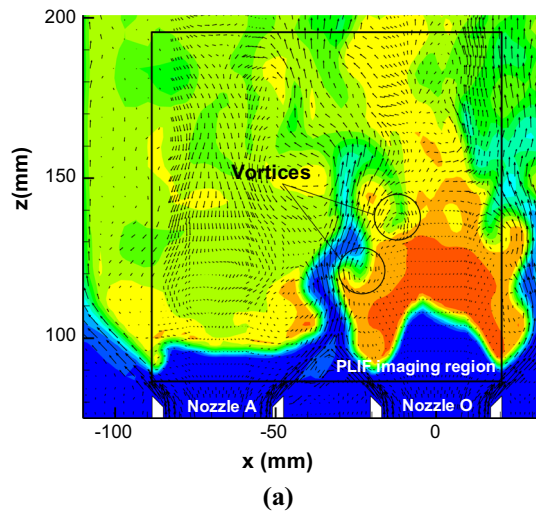


Fig. 11 **a** Instantaneous distribution of OH concentration calculated with LES in $y = 0$ plane at $\phi = 0.6$. **b** A snap shot of OH-PLIF of two neighboring flames with corresponding inlet condition (marked area in **a**)

4.2.2 Interaction of multi-nozzle flames

Flame light images of the CH_4/air premixed multi-nozzle flames are shown in Fig. 12. The flames for all five nozzles liftoff the nozzle exit, being blue in lean condition and light yellow when the equivalence ratio reaches 0.8. The mean flame front forms an bowl shape for each nozzles. The diameter and length of the visible flame are about 2.5 and 1.5 diameters of the nozzle, respectively. Note that the diameter of the center flame is a little smaller than that of the outer ones owing to the confinement by the other four nozzles. From the brightness of the flame in the regions between the center nozzle and outer nozzles, we can infer that the combustion is enhanced in the neighboring interacting zones.

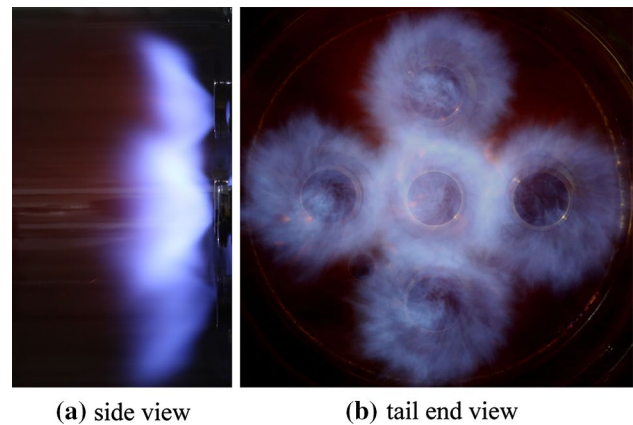


Fig. 12 CH_4 multi-nozzle flames at $\phi = 0.7$, $U_0 = 6.2$ m/s

Figure 13 shows mean OH radical distributions from PLIF at different equivalence ratios. For each case, the mean OH distribution is an average of 500 single-shot PLIF images. Ultra-high OH distributions are detected in interacting zone, which indicates that there is a part of premixed fuel burned in the interacting zones. As discussed above, vortices originated in the inner layer entrain premixed gases and move downstream to the interacting zones where the vortices collide with vortices from neighboring nozzle in the interacting zones creating a high turbulence flowfield. The highly intensive turbulence makes the flame highly wrinkled, increasing the heat release rate and the reaction rate of the premixed fuel.

It could be found that there are also OH distributions in the SRZ near the nozzle lips, which means that parts of the reactants burning in that region, producing a high-temperature region. The OH distribution becomes wider as the equivalence ratio increases. On the one hand, this is not desirable from the viewpoint of durability and reliability. On the other hand, the high-temperature region acts as a stable heat source, which may aid in the combustion stabilities of the multi-nozzle flames (Villalva 2013).

Neighboring swirling flows interact with each other, causing difference in flame stabilities of center and outer flames. From Fig. 13, we can find that the overall brightness of OH distribution above the outer nozzle is higher than the center nozzle for all cases, which means that the outer nozzle is more stable than the center one in multi-nozzle combustion. Figure 14 shows comparisons of mean OH radical distributions from PLIF and LES at $\phi = 0.5$. The overall shape of OH distribution is almost the same. The interesting observation is that almost no OH radical distributions are seen above the center nozzle when $\phi = 0.5$, meaning that the center nozzle is extinguished while the other four outer nozzles are still burning. This phenomenon is also successfully predicted by LES, which result shows that the

Fig. 13 Mean OH radical distributions of CH₄ multi-nozzle flames from PLIF at different equivalence ratios

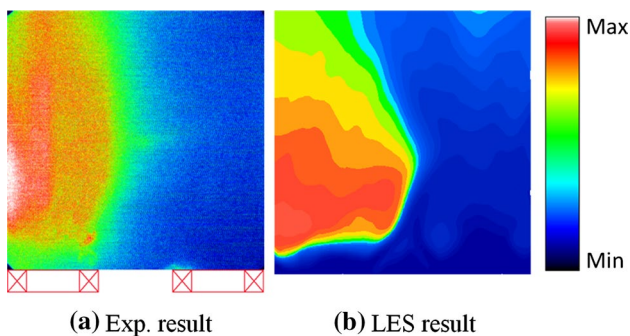
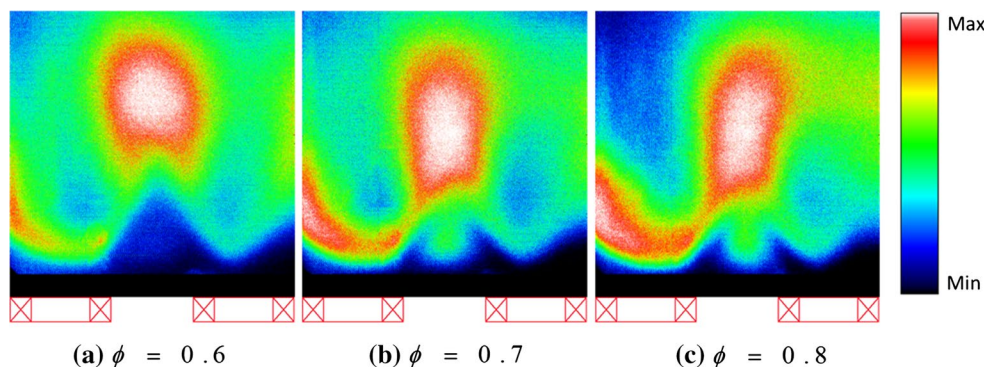


Fig. 14 Comparisons of mean OH radical distributions from PLIF and LES at $\phi = 0.5$

OH concentration above the center nozzle is nearly zero. This is mainly due to the confinement and distortion by the neighboring four outer nozzles, resulting in mismatch between the turbulent flame speed and the local flow velocity for center nozzle.

The flame propagates back and forth in the axial direction with the mean liftoff height of the flame being the mean equilibrium position above the burner. Figure 15 shows the mean liftoff height for different equivalence ratios with the same inflow velocity at the burner exit. The liftoff height determined in the experiment measurement is the maximum gradient of the OH signal at centerline, whereas the liftoff height from LES has been calculated as an average of the two lowest valleys of the flame surface and the flame surface position at nozzle axis. As shown in Fig. 15, the liftoff heights decrease with the increment of equivalence ratio both for measurement and LES except for $\phi = 0.5$. The liftoff height for outer nozzle at $\phi = 0.5$ is a little low due to a lack of interaction of the extinguished center nozzle flow. The liftoff heights of center flames are slightly higher than the outer neighboring ones for all cases. It also shows that reasonable agreement is found between simulations and experiments in terms of flame liftoff height.

Cheng et al. (2006) reports that the similarity features of divergent flow in the nearfield coupled with a linear

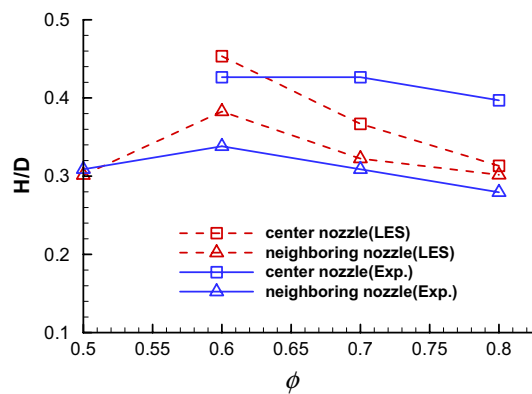


Fig. 15 Mean liftoff height from experiments and LES at different equivalence ratios with the same inlet velocity

correlation of S_T . It stems from a velocity balanced equation at the leading edge of the flame brush, x_f ,

$$1 - \frac{dU}{dx} \frac{(x_f - x_0)}{U_0} = \frac{S_L}{U_0} + \frac{Ku'}{U_0} \tag{17}$$

On the LHS, $dU/dx/U_0$ is the normalized axial divergence rate shown in Fig. 9a and x_0 is the virtual origin of divergent flow. On the RHS, S_L is the laminar flame speed shown in Table 2, K is an empirical constant that is in the order of 2.14 for methane, and u' is rms velocity of the turbulence. Since the similarity features of divergent flow, the normalized axial divergence rate, $dU/dx/U_0$, remains constant. Therefore, the x_f is mainly determined by the S_L and u' .

For multi-nozzle flames, because of the confinement and distortion of the neighboring flows discussed above, u' of the center nozzle flow is smaller than the adjacent flows although with the same structure. Hence, for the center nozzle, the RHS of the Eq. (17) is smaller, indicating the increment of the leading edge of the flame brush, x_f . This gives an explanation on why the center flame liftoff further downstream than adjacent nozzles. Similarly, high equivalence ratio means large laminar flame speed, which leads to the increment of RHS of Eq. (17). In contrast, x_f at LHS

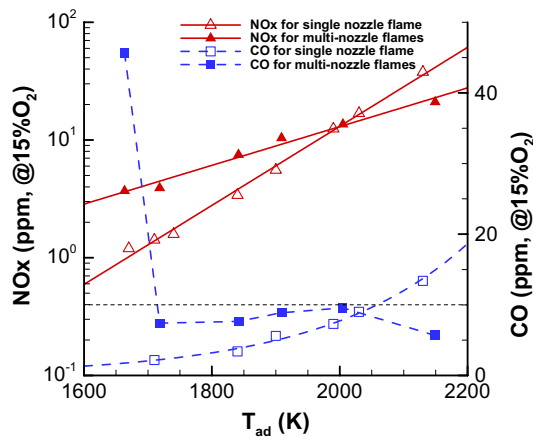


Fig. 16 Measurement of NO_x and CO emissions of low-swirl multi-nozzle flames fueled with CH₄

decreases. That is why the liftoff height of the premixed flames decreases as the equivalence ratio increases.

4.3 NO_x and CO emissions

The NO_x and CO emissions from CH₄ low-swirl multi-nozzle flames are given in Fig. 16. These measurements are made at a series of different equivalence ratios. Almost all of the NO_x emissions from CH₄ multi-nozzle flames are below 20 ppm and can even achieve single-digit emissions. As discussed previously, the lack of a strong recirculation zone and the shorter residence time may provide an explanation for the NO_x reduction. The NO_x emissions show log-linear dependency on the adiabatic flame temperature and are consistent with those for single low-swirl burner reported by Littlejohn et al. (2010). However, the rate of NO_x increment for multi-nozzle flame is lower than single burner, which means NO_x emissions for multi-nozzle flames are less sensitive to the flame temperature than those for single nozzle.

CO emissions of the multi-nozzle flames shown in Fig. 16 are well below 10 ppm for all cases studied in present experiments. The CO emissions for multi-nozzle flames are comparable to those for single burner. The high CO emission for the first case is due to combustion instabilities closing to lean blow-off limits. In all, the low-swirl multi-nozzle flames do not entail compromising CO for the sake of lowering NO_x.

5 Conclusions

A low-swirl multi-nozzle model combustor including five low-swirl nozzles was constructed. Large-eddy simulations and laser diagnostic experiments were performed on

the combustor at bulk flow velocity of 6.2 m/s for each nozzle. Results show that the neighboring swirling flows interact with each other, generating a highly turbulent interacting zone where intensive reactions take place. Multi-nozzle flames settle in the inner shear layer and the liftoff heights decrease with the increment of equivalence ratio. The center flow is confined and distorted by the neighboring flows in multi-nozzle combustor, resulting in instabilities of the center flame, especially closing to the lean blow-off limits. The center nozzle flame is extinguished at $\phi = 0.5$, which is successfully predicted by LES. Therefore, for multi-nozzle combustor with low-swirl burners working at lean premixed conditions, it is necessary to increase the center nozzle equivalence ratio properly or adopt diffusion pilot combustion method for the sake of combustion stability.

In addition, the low-swirl multi-nozzle combustion can achieve ultra-low emissions. NO_x emissions show log-linear dependency on the adiabatic flame temperature, while the CO emissions remain lower than 10 ppm. NO_x emissions for multi-nozzle flames are less sensitive to the temperature than those for single nozzle.

Acknowledgments This work was supported by the National Natural Science Foundation of China (Grant No. 51206109).

References

- Biagioli F, Güthe F, Schuermans B (2008) Combustion dynamics linked to flame behaviour in a partially premixed swirled industrial burner. *Exp Therm Fluid Sci* 32:1344–1353
- Boehm B, Dreizler A, Gnirss M, Tropea C, Findeisen J, Schiffer H (2007) Experimental investigation of turbulence structure in a three-nozzle combustor. In: *ASME Turbo Expo 2007*, GT2007-27111
- Cai J, Jeng SM, Tacina R (2001) Multi-swirler aerodynamics experimental measurements. In: *37th AIAA/ASME/SAE/ASEE joint propulsion conference and exhibit*, AIAA 2001-3574
- Cai J, Jeng SM, Tacina R (2002) Multi-swirler aerodynamics: comparison of different configurations. In: *Proceedings of ASME Turbo Expo*, GT2002-30464
- Chan CK, Lau KS, Chin WK, Cheng RK (1992) Freely propagating open premixed turbulent flames stabilized by swirl. *Proc Combust Inst* 24:511–518
- Cheng RK (1995) Velocity scalar characteristics of premixed turbulent flames stabilized by weak swirl. *Combust Flame* 101:1–14
- Cheng RK (2006) Low swirl combustion the gas turbine hand book. <http://prod75-inter1.netl.doe.gov/technologies/coalpower/turbines/refshelf/handbook/3.2.1.4.2.pdf>
- Cheng RK, Fable SA, Schmidt D, Arellano L, Smith KO (2001) Development of a low swirl injector concept for gas turbines. In: *International joint power conference*, IJPGC2001/FACT-19055
- Cheng RK, Littlejohn D, Nazeer WA, Smith KO (2006) Laboratory studies of the flow field characteristics of low-swirl injectors for adaptation to fuel-flexible turbines. In: *ASME Turbo Expo*, GT2006-90878
- Cheng RK, Littlejohn D, Strakey PA, Sidwell T (2009) Laboratory investigations of a low-swirl injector with H₂ and CH₄ at gas turbine conditions. *Proc Combust Inst* 32:3001–3009

- Day M, Tachibana S, Bell J, Lijewski M, Beckner V, Cheng RK (2012) A combined computational and experimental characterization of lean premixed turbulent low swirl laboratory flames I. Methane flames. *Combust Flame* 159:275–290
- Erlebacher G, Hussani MY, Speziale CG, Zang TA (1992) Toward the large eddy simulation of compressible turbulent flows. *J Fluid Mech* 238:155–158
- Johnson MR, Littlejohn D, Nazeer WA, Smith KO, Cheng RK (2005) A comparison of the flowfields and emissions of high-swirl injectors and low-swirl injectors for lean premixed gas turbines. *Proc Combust Inst* 30:2867–2874
- Kim J, Yoo K, Sung H, Zhang LW, Yang V (2010) A numerical study of flow dynamics in an annular combustor with multiple swirl injectors. In: 48th AIAA aerospace sciences meeting, AIAA 2010-583
- Lannetti A, Tacina R, Cai J, Jeng SM (2001) Multi-swirler aerodynamics—CFD predictions. In: 37th AIAA/ASME/SAE/ASEE joint propulsion conference and exhibit, AIAA 2001-3575
- Littlejohn D, Cheng RK, Noble DR, Lieuwen T (2010) Laboratory investigations of low-swirl injectors operating with syngases. *J Eng Gas Turb Power* 132:011502-1–011502-8
- Nazeer W, Smith K, Sheppard P, Cheng RK, Littlejohn D (2006) Full scale testing of a low swirl fuel injector concept for ultra-low NO_x gas turbine combustion systems. In: ASME Turbo Expo, GT2006-90150
- Nogenmyr K-J, Fureby C, Bai XS, Petersson P, Collin R, Linne M (2009) Large eddy simulation and laser diagnostic studies on a low swirl stratified premixed flame. *Combust Flame* 156:25–36
- Petersson P, Collin R, Lantz A, Aldén M (2011) Simultaneous PIV, OH-and fuel-PLIF measurements in a low-swirl stratified turbulent lean premixed flame. In: Proceedings of the European combustion meeting, pp 1–6
- Smith KO, Therkelsen PL, Littlejohn D, Ali S, Cheng RK (2010) Conceptual studies of a fuel-flexible low-swirl combustion system for the gas turbine in power plants. In: Proceedings of the ASME Turbo Expo, GT2010-23506
- Szedlmayer MT, Quay BD, Samarasinghe J, Rosa AD, Lee JG, Santavicca DA (2011) Forced flame response of a lean premixed multi-nozzle can combustor. In: ASME Turbo Expo 2011, GT2011-46080
- Villalva R (2013) Emissions and operability of a multi-point low NO_x staged combustor at intermediate pressures. In: ASME Turbo Expo, GT2013-95135
- Worth NA, Dawson JR (2012) Cinematographic OH-PLIF measurements of two interacting turbulent premixed flames with and without acoustic forcing. *Combust Flame* 159:1109–1126